A Ground-Based Sense-and-Avoid System for Small Unmanned Aircraft

Laith R. Sahawneh*
University of Florida, Shalimar, Florida 32579

Jared K. Wikle†
MIT Lincoln Laboratory, Lexington, Massachussetts 02421

Adam K. Roberts‡
Monovo, Salt Lake City, Utah, 84047

Jonathan C. Spencer§
Princeton University, Princeton, New Jersey, 08544

Timothy W. McLain¶, Karl F. Warnick‖, and Randal W. Beard**
Brigham Young University, Provo, Utah, 84602

In this article, we present a complete, proof-of-concept sense-and-avoid solution for small unmanned aircraft systems, including a small low-cost ground-based radar system, multi-target tracking and estimation, collision detection, and an avoidance planner. We describe the development of a small frequency-modulated continuous-wave phased-array radar system that provides a 3D surveillance volume. The radar measurements are processed using the recursive random sample consensus algorithm, producing tracks for the intruders and the ownship. We propose a collision-detection algorithm based on the geometric relationship between encountering aircraft. If a collision threat is detected, a collision-free new path is generated for the ownship using a two-step path-planning algorithm. In the first step, an initial suboptimal path is generated using an A* search. In the second step, the path is refined using a variant of the potential fields technique, adapted to the sense and avoid scenario. The performance of the complete system is demonstrated with flight test experiments.

Nomenclature

c_n = path planning path deviation cost

c_r = path planning collision risk cost

*Post-Doctoral Associate, Department of Mechanical and Aerospace Engineering, AIAA member
†Associate Staff
‡Systems Engineer
§Ph.D. Candidate, Department of Electrical Engineering
¶Professor, Mechanical Engineering, AIAA Associate Fellow
‖Professor, Electrical and Computer Engineering
**Professor, Electrical and Computer Engineering, AIAA Associate Fellow

c_t = path planning threat cost associated with an intruder

d = down location of target

d_{rd} = down location of radar station

d_s = diameter of cylindrical safety volume

d_{th} = horizontal collision distance threshold

e = east location of target

e_{rd} = east location of radar station

h_s = height of cylindrical safety volume

N_{bins} = number of radar frequency bins

N_s = number of radar samples

n = north location of target

n_{rd} = north location of radar station

P_{fa}^{i} = probability of false alarm for range bin i

$\tilde{p}_i$ = estimate of noise power for range bin i of each radar channel

$\mathbf{p}_j$ = inertial position of jth intruder

$\mathbf{p}_O$ = inertial position of ownship

$\boldsymbol{R}_i$ = correlation matrix for radar range bin i

$\bar{\boldsymbol{R}}_i$ = time averaged correlation matrix for radar range bin i

r = range to tracking target

S = return power function for range bin i

T_i = false alarm amplitude threshold for range bin i

t = current time

$t_{cpa,j}$ = time of closest point of approach for jth intruder

$\mathbf{v}_j$ = inertial velocity of jth intruder

$\mathbf{v}_O$ = inertial velocity of ownship

$\mathbf{x}$ = state vector for target motion model

$\mathbf{y}$ = measurement vector for target motion model

$\mathbf{w}(\alpha, \varepsilon)$ = return power weight vector for a particular azimuth and elevation angle pair

α = azimuth angle to tracking target

$\chi_k[i]$ = radar range compressed image from kth channel for range bin i

$\delta\mathbf{p}_j$ = position of jth intruder relative to ownship

$\delta\mathbf{v}_j$ = velocity of jth intruder relative to ownship

ε = elevation angle to tracking target

λ_i = inverse of expected value of noise power estimate for range bin i

σ_r = standard deviation of range measurement noise

σ_α = standard deviation of azimuth measurement noise

σ_ε = standard deviation of elevation measurement noise

τ = look-ahead time for collision detection

$\tau_{cpa,j}$ = time to closest point of approach for jth intruder

τ_{th} = collision time threshold

I. Introduction

An important goal of the unmanned aircraft systems (UAS) community is to achieve routine, safe, and affordable access to the national airspace system (NAS). The need to integrate UAS into the NAS is motivated by the rapid growth of the UAS industry, especially small UAS weighing less than 55 lb. Most research efforts have focused on technologies for integrating medium and larger UAS into the NAS. However, there are many potential civil and commercial applications for small UAS, including package delivery, precision agriculture, wildfire monitoring, border patrol, and infrastructure monitoring. As such, there is a significant need for sense and avoid technologies that are focused on small UAS.

With regard to UAS in the NAS, the Federal Aviation Administration (FAA) has mandated that UAS be capable of an equivalent level of safety to the see-and-avoid mandate for manned aircraft [1, 2]. As a result, a UAS must be capable of monitoring and avoiding other manned or unmanned aircraft in its vicinity, similar to a pilot's ability to visually scan the surrounding airspace, and then to respond appropriately so that the UAS remains well clear, and avoids collisions with other air traffic [3].

A complete sense and avoid system is comprised of sensors and associated trackers, collision detection algorithms, and a collision avoidance planner. The main role of the sensor and tracker is to detect air traffic and to track the motion of the detected aircraft to gain sufficient confidence that the detection is valid. Not every aircraft that is observed by the sensing system, however, presents a collision threat. The ownship should only maneuver to avoid intruders when a collision threat is imminent. Therefore, the collision detection system determines whether or not an approaching intruder is on a collision course. Once a collision threat has been detected, the collision avoidance system must plan the proper evasive maneuver.

A collision is declared when two or more aircraft are less than the minimum allowed horizontal and vertical distance, which is called the collision volume [4, 5]. A common specification for the collision volume is a horizontal distance of 500 ft and a vertical distance of 200 ft [3, 6, 7].

In general, the most suitable SAA configuration depends on the dynamic characteristics, size, weight, and power

(SWaP) resources, payload of the UAS airframe, and the nature of the mission. In this paper, we present a ground-based SAA system that consists of a ground control station that includes all sensors, communication, signal processing, and control logic.

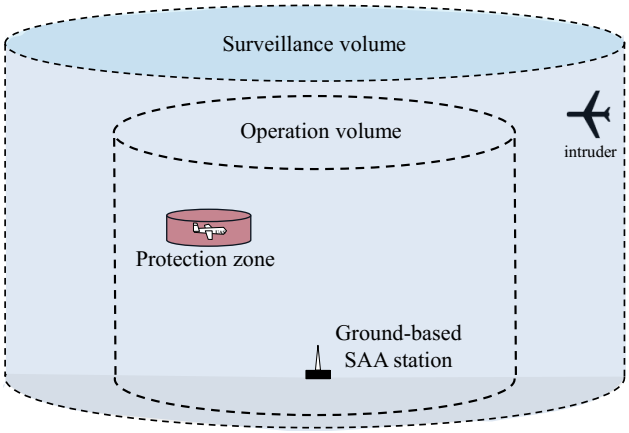

Fig. 1 Surveillance and operating volumes associated with the ground-based radar SAA system.

Figure 1 shows the typical operating volumes associated with a ground-based SAA system. In this configuration, the ground-based sensor detects air traffic in a fixed volume of airspace called the surveillance volume. The ownship flies in a volume of airspace referred as the operation volume. The size and geometry of the operation volume depends on (1) the minimum required detection range to be able to detect and track the intruder, (2) the time required to evaluate the encounter scenario, (3) the time required to plan an avoidance maneuver, and (4) the time required to take an evasive action. A drawback to using a ground-based SAA system is that it provides a static coverage volume, which may be less than the operating range of the UAS. Also, using ground-based SAA introduces the issue of maintaining a reliable, and efficient data link between the ground control station and the ownship. In addition, local terrain may also reduce the surveillance volume, and introduce noise in the measured information.

Various solutions exist for ground-based SAA, however, these solutions have limitations when applied to small UAS. One ground-based SAA system is the mobile aircraft tracking system (MATS) [8]. The MATS consists of a 2D primary radar, which provides range and azimuth information about targets, an ADS-B receiver and a transponding interrogator. The primary radar of the MATS has a peak output power of 25 kW and provides two modes of instrumented range: 54 nmi with resolution of 180 m or 27 nmi with resolution of 45 m. The performance of MATS was examined as part of the Smart Skies project using a specially equipped Cessna 172R. The main function of MATS is to detect and track intruding aircraft and provide this information to the UAS pilot located at the ground control station. In other words, the MATS system provides the sense element while the pilot evaluates the risk and performs the avoidance function if needed. Another example is the modern Thales Star 2000 air traffic control (ATC) radar that has a peak output power of 28 kW and provides a coverage of 100 nmi with resolution of 230 m. Similar to MATS it provides only

range and azimuth information about threats. The lack of elevation data is a limitation of the system. The MATS and Star 200 system assume low density traffic where 2D information is sufficient and another cooperative sensor provides the altitude information to supplement the radar data [4]. The sense-and-avoid display system (SAVDS) which uses the Sentinel AN/MPQ-64 air defense radar is a ground-based SAA system that is capable of providing 3D information about targets. It has a peak output power of 23 kW and provides a coverage of 40 nmi with resolution of 150 m [4]. In general, traffic control radar and high-tech military radars tend to be very expensive. For example, the cost guide of the terminal maneuvering area radar is 8 million U.S. dollars [9].

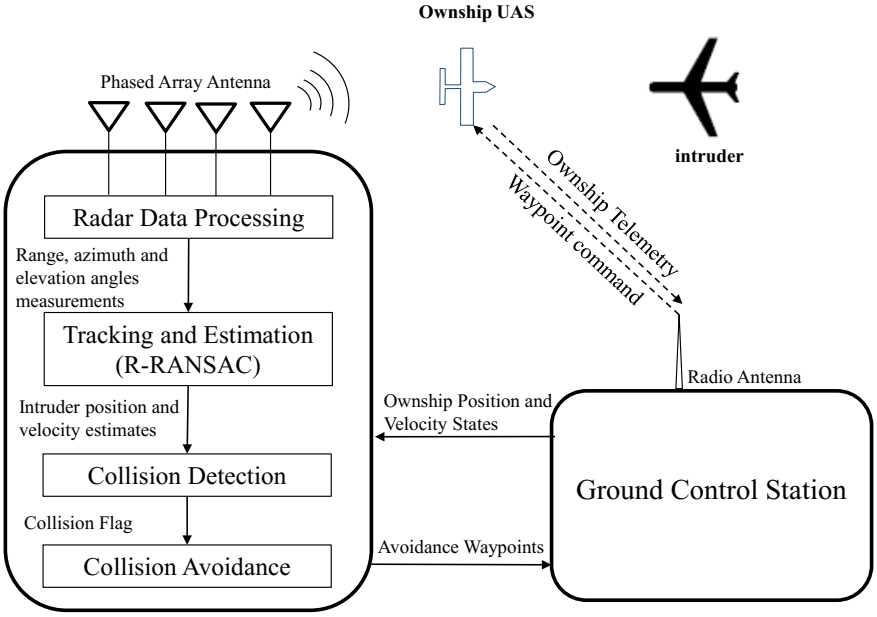

Fig. 2 Ground-based radar sense-and-avoid system structure diagram.

The key contribution of this paper is to present a complete, proof-of-concept ground-based sense-and-avoid solution that is feasible for small UAS. This system uses a reliable ground-based radar sensor, tracking and estimation algorithms, collision detection algorithms, and a collision avoidance scheme. As shown in Figure 2, radar returns from all of the targets are received by a phased-array antenna. The radar data is processed to produce range and azimuth and elevation angles to all targets. In the tracking step, the target's measurements are processed using the recursive-RANSAC (R-RANSAC) algorithm [10] to estimate the state of potential intruders, and to distinguish the ownship. After R-RANSAC filtering, the time to closest point of approach (CPA) and the distance at CPA are computed to identify possible collisions. If a collision threat is detected, the intruder position and velocity estimates and an activation flag are passed to the collision avoidance algorithm. Once the collision level of the avoidance logic has been activated, a new collision-free path is generated using a two-step collision avoidance algorithm. In the first step, an initial suboptimal path is generated using A* search. In the second step, a simulated chain of unit masses connected by springs and dampers evolves in a simulated force field. The chain is described by a set of ordinary differential equations

that is driven by virtual forces to find the steady-state equilibrium. The final output of the SAA system is a revised set of waypoints that are transmitted to the ownship. The system shown in Figure 2 is a complete SAA system for small UAS. It is viable for both fixed wing and multirotor aircraft, and could reasonably be extended for larger UAS outside of the small UAS definition.

The rest of the paper is organized as follows. Section II describes the ground-based sensor system. The target tracking and management algorithm is presented in Section III. Section IV proposes a geometric-based approach to detect collisions with encountering intruders. Section V presents the two-step collision avoidance algorithm. Flight test results are discussed in Section VI, while Section VII concludes the paper.

II. Ground-Based Sensor

For sense and avoid systems, radar has many advantages over other sensors like EO/IR cameras, lidar, and ultrasound. In particular, radar has inherently good range resolution and functions in diverse weather and lighting conditions [11]. However, small UAS present a unique sensing challenge. Whereas general aviation happens at higher altitudes where they are far removed from sources of clutter, small UAS fly below 500 ft near the surface of the earth.

Modern air traffic control (ATC) radars use large ground-based systems that can detect aircraft approaching from up to 400 km away [12]. These radar systems achieve a long detection range by using large, high-gain antennas to focus the radar energy into beam widths ranging from 2 to 5 deg. The antennas are placed on large mechanical gimbals that rotate the antenna to scan the narrow beam. Since most aircraft fly at predictable altitudes, these systems scan over a relatively narrow set of angles vertically, while providing 360 deg of horizontal coverage. Although the large antennas and high transmitted power permit long-range detection, the system has a doughnut shaped detection pattern that is blind to targets directly overhead. These systems also avoid scanning too close to the horizon to avoid ground clutter reflections from man-made structures.

Although miniature scale versions of current ATC radar exist, they are not viable for small UAS because they provide only two-dimensional sensing where UAS sensing requires three-dimensional spatial localization. Gimballed radar systems not only have blind-spot issues overhead, but their update rate is very slow: on the order of a few seconds [4]. For long-range radar systems, this is not an issue since their detection range is long enough to compensate for a slow update rate, but for short-range radar systems, aircraft could travel most of the way through the field of view in a single update interval. A solution to resolve the issues of a mechanically steered antenna is to replace it with an electronically steered array (ESA) of antennas. An ESA or phased-array antenna has the same narrow beam and high resolution as a mechanically steered antenna, but it can be steered with a wider field of view and a much higher update rate.

A potential solution for ground-based collision avoidance sensors for UAS is to create a planar phased-array radar with a wide field of view angled directly at the sky as shown in Fig. 3(a). This would create a 3D hemispherical bubble where the radar can detect targets and guarantee safe flight within the bubble. The update rate for a phased-array radar

that implements digital beam forming is the pulse rate of the system, which is on the order of milliseconds. As a result, such a system can provide high resolution in range, elevation angle, azimuth angle, and time. The field of view of these planar phased-array systems covers the full extent of UAS flight paths, and can implement filtering methods to remove background reflections from the environment.

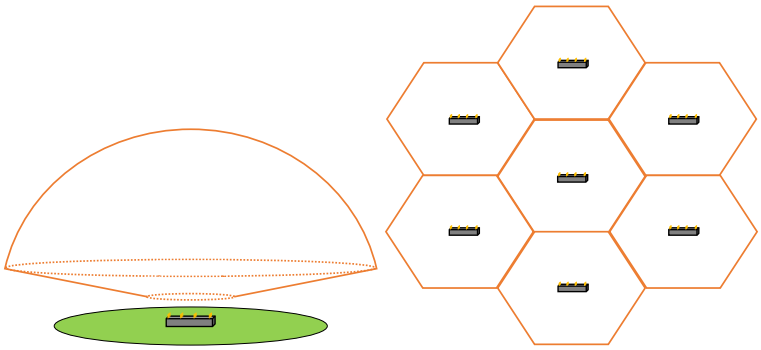

(a) 3D surveillance volume of a single planar phased-array radar

(b) Radar Network Cells

Fig. 3 UAS surveillance using planar phased arrays.

To expand the coverage of the radar along the ground, multiple radar systems could be arranged into a grid similar to the current cell phone antenna network. This configuration, shown in Fig. 3(b), is designed to establish coverage over a wide area while maintaining low radiated power and ensuring that a single antenna is not overwhelmed with traffic. Since UAS only need to know about nearby air traffic, this cellular radar sensor network also provides an efficient solution to manage the volume of data produced by air traffic monitoring. A maneuvering aircraft will communicate only with nearby radar sensors to obtain local air traffic information rather than being required to communicate with a central source that transmits global air traffic. This type of a system is scalable depending on the amount of air traffic expected. In rural areas, the cells could be very large or the system could just use on-board sensors for collision avoidance since little intruding traffic is expected. In densely populated urban environments where a lot of traffic is expected cells could be made smaller to ensure adequate coverage and load balancing.

The system described in the previous paragraphs is feasible using currently available technology. While radar systems of the past have typically been large and cumbersome, being made up of bulky waveguides and heavy ferrite components, progress in microwave integrated circuits has driven down the cost and the size of radar systems to create a new class of small, short range, low power, low cost systems [13]. While automotive applications make up the majority of these systems, there is a growing body of work using small frequency modulated continuous wave (FMCW) radar systems in UAS sensing. Kemkemian et al. proposed a MIMO radar architecture for UAS sensing to to determine angle of arrival information in elevation and azimuth [14, 15]. Itcia et al. implemented a SAA radar on a Cessna that was capable of detecting larger aircraft using floodlight illumination and digital beamforming receiver for a fully static

system [16]. Shi et al. produced a similar system using off the shelf components that demonstrated good performance in bench-top testing [17].

Radar inherently has high resolution in range but poor resolution in angle, which is why it requires a phased-array antenna to provide that information. Antennas arranged in a regular pattern use the propagation path difference between elements as a way of determining the direction of arrival of a target. A phased array forms a beam in a particular direction by multiplying the antenna outputs by pre-calculated weights and summing the outputs to produce a single result that simulates an antenna pointed in that direction. In systems where receivers are costly, this beamforming occurs directly at the antenna output and is referred to as analog beamforming. In systems such as this one where the cost of adding multiple receiver channels is low, the beamforming occurs after the signal has been digitized and is referred to as digital beamforming. Analog beamforming allows the system to steer the beam much more rapidly than a mechanical gimbal. Digital beamforming allows the user to form many beams and track multiple targets at different angles simultaneously.

A phased-array radar sensor offers many advantages for SAA detection in UAS applications. Using a ground-based phased-array radar frees up payload requirements on UAS. A planar phased array also can provide fast update rates as well as accurate angle and range information. Finally, using smaller, low-power, and short-range systems, such as the planar phased-array FMCW radar design described in this paper, enable a scalable, low-cost radar network to provide surveillance capabilities required for SAA detection. The flight results presented in Section VI use a preliminary prototype of this radar, a four-channel phased-array system that scans only in the azimuth direction.

III. Target Tracking and Track Management

In this section we address the major components of target tracking and multi-track management.

A. Front-End Signal Processing

The signal produced by an FMCW homodyne radar is a sum of sinusoids of different frequencies, where each frequency corresponds to a target's range. The signal is sampled and the FFT is used to produce a range compressed image (RCI) for each radar pulse. Each RCI is composed of the positive frequency bins of the FFT, where the number of bins is $N_{\text{bins}} = N_s/2$ and each frequency bin is proportional to a specific range bin. The sampling and FFT are performed on each of the N_c receiver channels.

Letting $\chi_k[i]$ denote the RCI from the kth channel for range bin i, and letting

$$\boldsymbol{\chi}[i] = \begin{bmatrix} \chi_1[i] & \chi_2[i] & \dots & \chi_{N_c}[i] \end{bmatrix}^\top, \tag{1}$$

then the correlation matrix for each range bin is

$$\boldsymbol{R}_i = \chi[i]\chi^H[i]. \tag{2}$$

To increase the signal-to-noise ratio (SNR) of the targets, N_{avg} correlation matrices, from consecutive radar pulses, are averaged to form the averaged correlation matrix $\bar{\boldsymbol{R}}_i$.

Using these averaged correlation matrices, target range detection is performed. Targets are detected by setting an amplitude threshold based on the noise statistics of the radar. The detection system then discriminates between targets and non-targets based on whether a particular return rises above the threshold or not. The radar system sets a threshold based on the estimate of the noise power in each range bin [18]. In this threshold method, the estimate of the noise power $\tilde{p}_i$ for each of the N_c channels in the ith range bin is computed by saving multiple $\bar{\boldsymbol{R}}_i$ in a noise-only environment, averaging over an N_{save} window, and then computing the mean of the diagonal elements of $\bar{\boldsymbol{R}}_i$. The estimate of the noise power $\tilde{p}_i$ is given by

$$\tilde{p}_i = \frac{1}{N_c} \sum_{j \leq N_c} \bar{\boldsymbol{R}}_i[j, j]. \tag{3}$$

The noise statics of each range bin follows an exponential probability distribution, $\Pr(\chi_k)=\lambda_i \exp^{-\lambda_i \tilde{p}_i}$, where $\lambda_i=1/E\{\tilde{p}_i\}$ is the inverse of the expected value of the noise power estimate for each range bin [19]. By using this noise power estimate to calculate the exponential parameter λ_i for each range bin, the probability of false alarm for each range bin is given by [19]

$$P_{fa}^i = \exp\left(-\lambda_i T_i\right), \tag{4}$$

where T_i is the amplitude threshold. Then, by choosing an appropriate value for the probability of false alarm for each range bin, we solve for T_i in Eq. (4) as

$$T_i = \frac{\ln(1/P_{fa}^i)}{\lambda_i}. \tag{5}$$

Finally, digital beamforming is used to obtain the azimuth and elevation angles to each target. The return power as a function of the ith range bin, azimuth angle α, and elevation angle ε is given by

$$S(r, \alpha, \varepsilon) = \mathbf{w}^H(\alpha, \varepsilon)\bar{\mathbf{R}}_i \mathbf{w}(\alpha, \varepsilon), \tag{6}$$

where $\mathbf{w}(\alpha, \varepsilon)$ is the weight vector for a particular azimuth and elevation angle pair (α, ε). The bearing angle with the greatest returned power is used as the estimate of the target's azimuth and elevation angles.

B. Multiple Target Tracking

One of the requirements of a SAA system is the ability to detect and track multiple targets. There are numerous multiple target tracking (MTT) algorithms available in the literature. In this paper we use the recursive-RANSAC algorithm developed by Niedfeldt [20–24], that has several advantages over existing MTT algorithms. The SAA problem for small UAS requires that the MTT algorithm includes track management, is robust to clutter and missed measurements, and is computationally efficient. Competing algorithms do not include all of these features. For example, the global nearest neighbor [25], (joint) probabilistic data association filters [26] [27], and particle filters [28] do not include track management. The probabilistic hypothesis filter [29, 30] is not robust to missed measurements, and the multiple hypothesis tracking filter [31] is not computationally efficient.

The R-RANSAC algorithm retains in memory all measurements from the past N_w time steps and uses a stochastic search algorithm to find trajectories that fit the data over the time window. The data is fit using a Kalman filter using an assumed motion model given by

$$\begin{aligned} \mathbf{x}[k] &= A\mathbf{x}[k-1] + \xi[k], \\ \mathbf{y}[k] &= C\mathbf{x}[k] + \eta[k], \end{aligned} \tag{7}$$

where $\xi[k]$ and $\eta[k]$ are zero-mean Gaussian random vectors with known covariance. For this paper we assume that the targets move with nearly constants acceleration, implying that the state $\mathbf{x} \in \mathbb{R}^6$ is composed of the inertial position and velocity of the target. Accordingly, the system matrices are given by

$$\begin{aligned} A &= \begin{pmatrix} \mathbf{I}_{3\times3} & \Delta t\mathbf{I}_{3\times3} \\ \mathbf{0}_{3\times3} & \mathbf{I}_{3\times3} \end{pmatrix} \\ C &= \begin{pmatrix} \mathbf{I}_{3\times3} & \mathbf{0}_{3\times3} \end{pmatrix}, \end{aligned}$$

where we have assumed that the radar measurements of range r, azimuth α, and elevation ε, have been converted to NED coordinates using

$$\begin{aligned} n &= r\cos(\alpha)\cos(\varepsilon) + n_{rd}, \\ e &= r\sin(\alpha)\cos(\varepsilon) + e_{rd}, \\ d &= r\sin(\varepsilon) - d_{rd}, \end{aligned} \tag{8}$$

where $(n_{rd}, e_{rd}, d_{rd})^\top$ is the NED location of the radar station.

One of the issues that arise when using the transformed measurement in Equation (8) is that the noise characteristics

of the radar cannot be accurately transformed into the NED coordinate frame. This is a problem because the noise characteristics are used in the R-RANSAC algorithm to decide if a new measurement is an inlier to an existing model. The noise characteristics in the range, azimuth, and elevation frame can be described as an inverted shallow bowl as illustrated in Figure 4. As the range to the target increases the diameter of this bowl also increases because σ_α and σ_ε remain constant. This means that the noise in the north, east, and altitude directions grows with range, and the relative noise among the three directions changes depending on the azimuth and elevation angles.

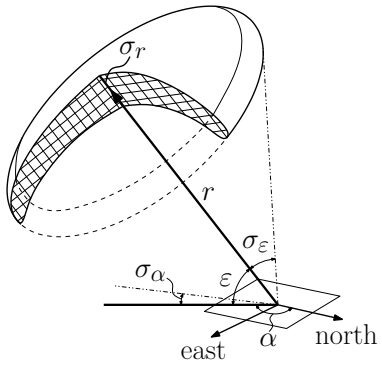

Fig. 4 Covariance of radar measurements.

The solution is to convert the NED coordinates of the existing tracks to range, azimuth, and elevation using

$$\begin{pmatrix} r \\ \alpha \\ \varepsilon \end{pmatrix} \triangleq \begin{pmatrix} \sqrt{n^2 + e^2 + d^2} \\ \tan^{-1}\left(\frac{e}{n}\right) \\ \sin^{-1}\left(\frac{-d}{\sqrt{n^2+e^2+d^2}}\right) \end{pmatrix}, \tag{9}$$

and then to determine if the current measurement is an inlier to the existing track, using σ_r, σ_α and σ_ε.

Another modification is needed to make the R-RANSAC algorithm work with a ground-based radar SAA scenerio. Since a ground-based radar will provide measurements for all aircraft in its field of view, measurements of the ownship will be sent to the R-RANSAC algorithm, a track will be created for the ownship, and the ownship track will be identified as an intruder. If the ownship is identified as an intruder, the path planner will create an avoidance path causing the ownship to deviate from its path when such a maneuver is not necessary. The modification made within R-RANSAC is to use the ownship's known states, received from the data link between the ownship and the ground control station, as a second set of measurements that is used to identify the track corresponding to the ownship.

IV. Collision Detection

Collision detection is a challenging problem due to inherent noise, errors in prediction, and modeling the uncertain dynamics and intent of intruding aircraft [32–36]. Moreover, limited on-board computational resources, fast closing

speeds, and unanticipated maneuvers make it challenging to detect collisions without excessive false alarms.

The purpose of computing the collision risk is to determine an alert threshold value that triggers the initiation of an evasive maneuver to avoid an imminent collision with the detected intruding aircraft. A number of collision detection methods have been suggested in the context of air traffic management, mobile robotics, and autonomous control. Recent surveys on this topic include Kuchar & Yang [37], Albaker & Rahim[38], and Angelov [4]. Many of these approaches can either be classified as geometric or probabilistic, where each approach has different techniques to deal with errors. In the geometric approach, the collision risk is based on the geometric relationship between aircraft. Aircraft trajectory predictions are based on linear projections of current aircraft states such that the uncertainty of the predicted trajectory is translated into areas around the predicted trajectory referred to as safe zones. Linear projections are computationally efficient and prediction errors are negligible over short time horizons [39, 40] or assumed known when flight plans are communicated [41]. On the other hand, probabilistic methods estimate the probability of collision based on a probabilistic model of future intruder dynamics. The event probability is then compared to a certain threshold above which the aircraft is deemed to be in collision. These probabilities can be estimated using approximate analytical solutions [42], numerical approximation [43, 44], or Monte Carlo methods [45–47]. The expected utility is another approach used to develop a risk alerting system that accounts for future changes in alerts [48]. In general, probabilistic approaches are computationally intensive but suffer from fewer false alarms than geometric approaches.

In this paper, we use a simple collision detection logic that assumes that both the intruder and ownship are following straight-line paths. The collision logic is continually updated to account for scenarios where this assumption is violated. Let $\delta\mathbf{p}_j = \mathbf{p}_j - \mathbf{p}_O$ be the position of the jth intruder relative to the ownship, and let $\delta\mathbf{v}_j = \mathbf{v}_j - \mathbf{v}_O$ be the relative velocity, where $(\mathbf{p}_j, \mathbf{v}_j)$ and $(\mathbf{p}_O, \mathbf{v}_O)$ are the inertial positions and velocities of the jth intruder and ownship respectively. If t is the current time, and τ is the look-ahead time, then the relative position of the intruder at future time $t + \tau$ is given by

$$\delta\mathbf{p}_j(t + \tau) = \delta\mathbf{p}_j(t) + \tau\delta\mathbf{v}_j(t).$$

The time to the closest point of approach denoted as τ_{cpa} is defined as the future time instant at which the relative distance between aircraft is at a minimum. Assuming that the future flight paths of both aircraft are a straight line, the point of closest approach is calculated by finding τ so that $\left\|\delta\mathbf{p}_j(t + \tau)\right\|$ is minimized. By simple calculus we get that

$$t_{cpa,j} = \begin{cases} \dfrac{-\delta\mathbf{p}_j^\top \delta\mathbf{v}_j}{\|\delta\mathbf{v}_j\|^2} & \text{if } \left\|\delta\mathbf{v}_j\right\| \neq 0, \\ 0 & \text{otherwise.} \end{cases} \tag{10}$$

Note that $t_{cpa,j}$ will be zero when the relative position vector $\delta\mathbf{p}_j$ is perpendicular to the relative velocity vector $\delta\mathbf{v}_j$. The product $\delta\mathbf{p}_j^\top \delta\mathbf{v}_j$ characterizes whether or not the two aircraft are converging ($\delta\mathbf{p}_j^\top \delta\mathbf{v}_j < 0$), or diverging

($\delta\mathbf{p}_j^\top \delta\mathbf{v}_j > 0$). A negative closest point of approach implies that the aircraft are diverging from each other.

The standard choice of the protection zone is a cylindrical volume with radius d_s and height h_s. Accordingly, the horizontal and vertical range to the target at future time $t + \tau$ is given by

$$d_j(t+\tau) = \left\|(\mathbf{I}_{3\times 3} - \mathbf{k}\mathbf{k}^\top)(\delta\mathbf{p}_j(t) + \tau\delta\mathbf{v}_j(t))\right\|$$
$$h_j(t+\tau) = \left\|\mathbf{k}^\top(\delta\mathbf{p}_j(t) + \tau\delta\mathbf{v}_j(t))\right\|,$$

where $\mathbf{k} = (0\ 0\ 1)^\top$.

To predict whether or not the collision will occur for each intruder within the sensor range, we use the collision detection logic listed in Algorithm 1. In Algorithm 1, the horizontal distance threshold d_{th} and the time threshold τ_{th} are design parameters that define the collision avoidance threshold. The collision avoidance threshold is a variable boundary around the ownship, larger than the collision volume and depends not only on distance, but time and other factors [49, 50]. Line 2 in Algorithm 1 checks whether the current horizontal range $d_j(t)$ to the intruder is less than a horizontal threshold distance d_{th}, or if the intruder is converging and the time to CPA is below a time threshold τ_{th}. Line 3 checks to see if the horizontal and vertical distances at the predicted CPA are below the minimum safe distances d_s and $h_s/2$, respectively. If so, then line 4 initiates a collision avoidance maneuver.

Algorithm 1 Collision detection algorithm

1: **for** each jth intruder within sensor range **do**
2: **if** $\left\|\delta\mathbf{p}_j\right\| \leq d_{th}$ or ($\delta\mathbf{p}_j^\top \delta\mathbf{v}_j < 0$ and $t_{cpa,j} \leq \tau_{th}$) **then**
3: **if** $d_j(t + \tau_{cpa,j}) \leq d_s$ and $h_j(t + \tau_{cpa,j}) \leq h_s/2$ **then**
4: Initiate avoidance maneuver.
5: **end if**
6: **end if**
7: **end for**

V. Collision Avoidance Planning

Once a collision threat has been detected, the collision avoidance system must select the proper evasive maneuver. The essential requirement for the collision avoidance algorithm is to perform the avoidance maneuver so that the distance at the closest point of approach to the intruder is equal to, or greater than a minimum required safe distance. There are many different options for path planning for collision avoidance, and numerous algorithms have been proposed [35, 51–58]. In this paper, we use the two-step collision avoidance algorithm proposed in [59]. The basic idea is to use a high-level deliberative planning technique that updates a set of high-level waypoints on a relatively slow time scale, and then refines that waypoint path with a low-level reactive planner that accommodates the vehicle dynamics and reacts to wind and unexpected motion of the intruders on a relatively fast time scale. Therefore, the path-planning approach taken in this paper consists of two steps. In the first step, an initial suboptimal path is generated using an

A* search. In the second step, a chain of unit masses connected by springs and dampers evolves in a simulated force field, using the A* solution as an initial condition. The chain is described by a set of ordinary differential equations that is driven by virtual forces to find the steady-state equilibrium.

The A* algorithm is a widely used graph-based search method that uses an admissible heuristic to guide the search for a minimum-cost path between an initial node and one or more possible goal nodes. The A* algorithm is proven to be complete subject to the resolution of the grid employed and will always find a solution if one exists [60]. A drawback of A* search is that it is inherently a static algorithm, which means that when the workspace changes the previous path is no longer valid and the A* algorithm must replan from scratch. For the collision avoidance problem, the airspace around the ownship is represented by a grid of regularly sized cells. The ownship and intruders are localized to a specific cell, and the nominal ownship path is represented as sequence of connected cells. Unlike many path planning methods that use A* search, the nodes of the graph must take into account timing information. Therefore, a node on the graph is uniquely defined by its position, and the time of potential arrival of the ownship to that cell. The algorithm expands a position cell by determining the surrounding cells that are reachable from the current cell, and then determining the average time to transition between cells. In our current implementation, we assume that altitude can only change when the aircraft is flying straight ahead.

The segment cost of moving from a cell centered at $\mathbf{w}_a$ to a cell centered at $\mathbf{w}_b$ is given by

$$g\left(\mathbf{w}_a, \mathbf{w}_b\right) = k_d \|\mathbf{w}_b - \mathbf{w}_a\| + k_t c_t(\mathbf{w}_b, \mathbf{p}_j) + k_n c_n + k_r c_r, \tag{11}$$

where $\|\mathbf{w}_b - \mathbf{w}_a\|$ is the Euclidian distance between $\mathbf{w}_a$ and $\mathbf{w}_b$, $c_t(\mathbf{w}_b, \mathbf{p}_j)$ is the threat cost that intruder j exerts on cell $\mathbf{w}_b$, c_n is the cost of deviating from the original path, c_r is the risk of collision, and k_d, k_t, k_n, and k_r, are positive gains [59]. The final cost for the cell centered at $\mathbf{w}_b$ is given by

$$e(\mathbf{w}_b) = g\left(\mathbf{w}_a, \mathbf{w}_b\right) + \left\|\mathbf{w}_b - \mathbf{w}_f\right\|,$$

where $\mathbf{w}_f$ is the center of the cell that contains the nominal path when it leaves the local A* grid, and the last term is the heuristic that guides the A* search. Figure 5(a) and 5(c) show the results of the A* algorithm for a single intruder.

The second step of the collision avoidance planner is a chained-based potential field planner that explicitly takes timing information into account. Once an initial path has been generated by the A* algorithm as shown in Figures 5(a), and 5(c), it is superimposed by a chain of unit masses that are connected to one another by springs and dampers. The chain-based method is employed for two reasons. The first is to smooth the initial path generated by the A* algorithm, and the second is to dynamically react to changes in the environment. The basic idea is to impose forces on each mass in the chain based on the predicted location of the intruders, assuming that the intruder follows a straight-line path from

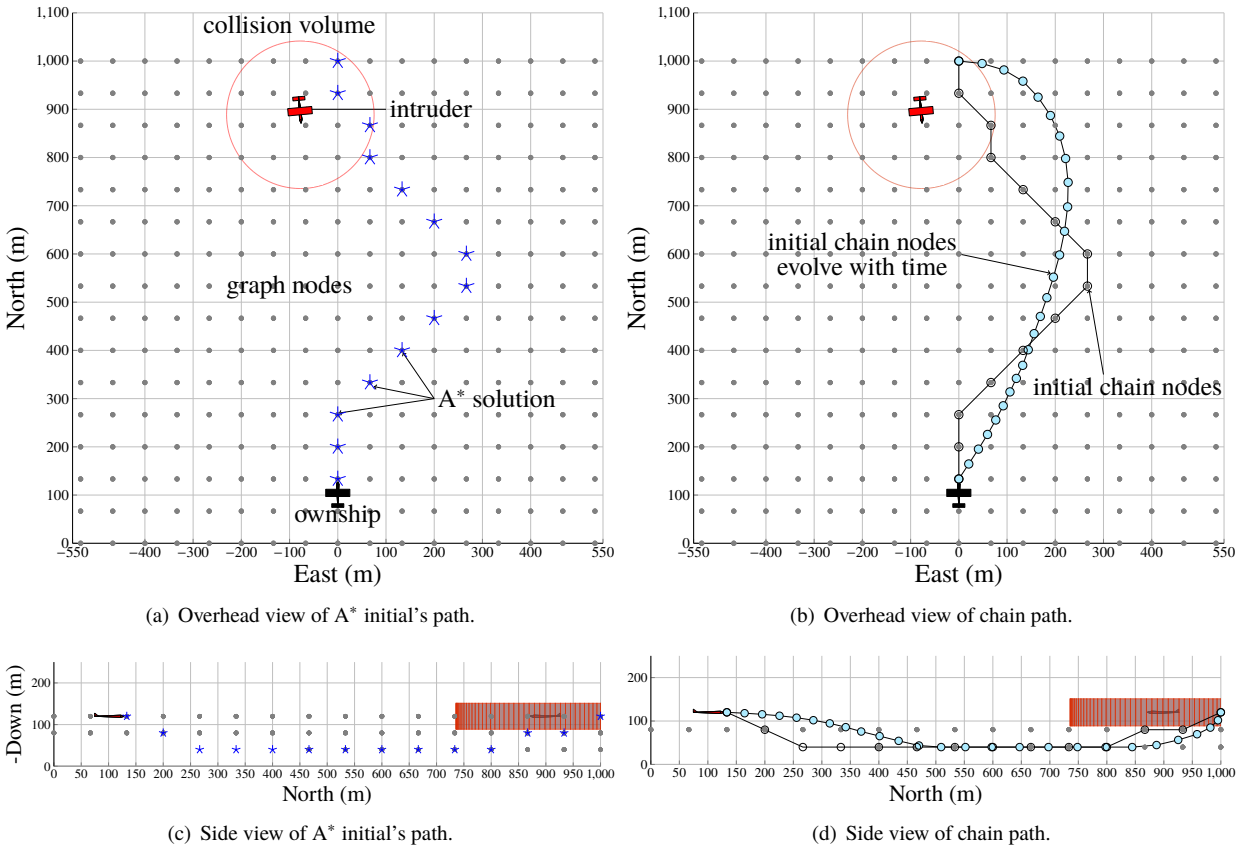

(a) Overhead view of A* initial's path.

(b) Overhead view of chain path.

(c) Side view of A* initial's path.

(d) Side view of chain path.

Fig. 5 The chain-based collision avoidance initialized by the A* algorithm.

its current location. Additional forces are imposed on the elements of the chain to ensure that turning rate constraints and flight-path angle constraints are respected. Additional details for the chain-based planner are given in [59]. The final results of the chain-based planner for one intruder are shown in Figures 5(b) and 5(d).

VI. Flight Results

The algorithms described in this paper have been extensively tested in simulation and results are described in [19]. In this paper, we will focus on hardware implementation and flight results that demonstrate the performance of the proposed ground-based radar sensor, R-RANSAC estimation scheme, collision detection, and collision avoidance algorithms. We used a 3D Robotics (3DR) X8 multicopter for the ownship and two 3DR Y6 multicopters for the intruders. A high-level depiction of the flight experiments is shown in Figure 6. Both the ground control station and the radar sensor are fixed on a platform that is positioned 1.83 m above the ground with the radar sensor is angled up by 3 deg to reduce ground clutter. All multicopters are flying at a constant altitude of 4.5 m above ground, and their start locations are roughly 50 m apart from each other. In addition, we have attached a corner reflector on each of the multicopters to enhance the radar cross section (RCS), and hence improved radar detectability.

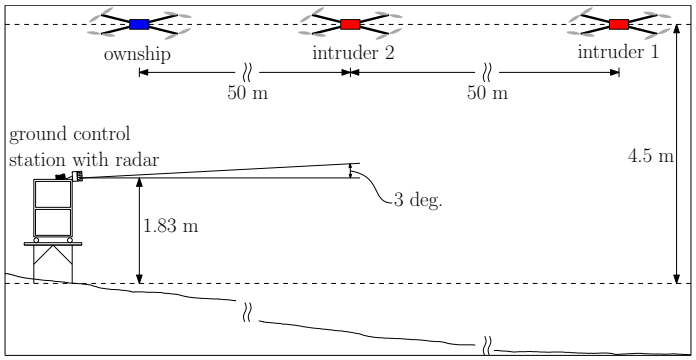

Fig. 6 Sketch of the encounter geometry of flight test (not to scale).

In this experiment, the R-RANSAC algorithm, the collision detection and avoidance algorithms, the interface module with the radar hardware, and communication with the ownship multicopter are implemented in Matlab/Simulink on a Lenovo Intel core i5 processor. The experimental setup is depicted in Figure 7. The telemetry of the ownship including position and velocity states and the avoidance waypoints are communicated between the ground-station laptop and the Pixhawk autopilot on-board the ownship using MAVLink message protocol over a 915 MHz 3DR telemetry radio set. The radar measurements are received through a wired connection with the laptop and read into Matlab/Simulink using a UDP receive block.

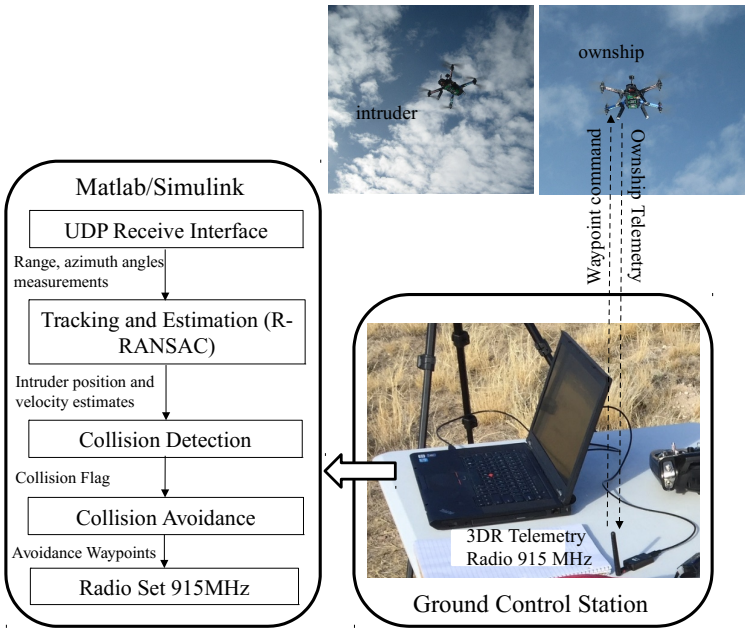

Fig. 7 The ground-based radar SAA experiment structure diagram.

In the flight test, we used a compact 2D line-array radar system that provides range and azimuth information about targets. The radar system is shown in Figure 8 and the key design parameters are listed in Table 1. It worth noting that this radar sensor was initially designed for an airborne SAA system for small UAS [61–63]. The main design objectives

were to minimize SWaP, and to provide a reasonably large field-of-view of approximately 120 deg horizontally and 30 deg vertically.

Table 1 Radar Sensor Parameters

Parameter	**Value**	**Parameter**	**Value**
Weight	120 g (0.26 lb)	Size	2.25 in x 4 in x 1 in
Consumed power	12 W	Transmitted power	250 mW
Center frequency	10.25 GHz	Radio frequency bandwidth	500 MHz
Sweep duration	2.048 ms	Intermediate frequency bandwidth	1 MHz
System noise figure	6 dB	Antenna elevation beamwidth	18 deg
Antenna gain	12 dB	Antenna azimuth beamwidth	80 deg
Array steerable range	120 deg	Number of receive elements	4
Peak channel coupling	approx. −20dB	Synthesized azimuth beamwidth	25 deg

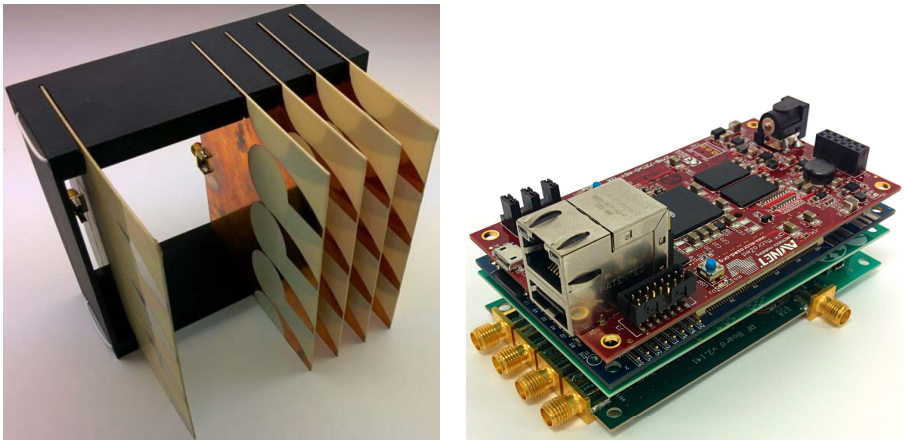

(a) Single transmitting and four-channel phased-array receiving antennas.

(b) Radar system processing boards.

Fig. 8 Portable 10 GHz FMCW phased-array radar system.

During the flight test, the radar processing board was used for digital signal processing. In the future, this board will also run the R-RANSAC tracking, collision detection, and collision avoidance algorithms. From the radar processing boards, the radar measurements were sent to a laptop, that served as a ground control station and also ran the tracking, collision detection, and collision avoidance algorithms. Since the current radar hardware is only capable of providing angular measurements in the azimuth direction, the altitude of the tracked targets is unobservable. Therefore, we assumed that each of the aircraft were flying at a constant known altitude.

The radar system uses a single transmitting antenna and a four-channel phased-array receiver that scans the azimuth angle as shown in Figure 8(a). The beamwidth of the synthesized beam varies from approximately 25 deg when steered at boresight to 32 deg when steered near the edge of field of view. Since these beamwidths are quite wide and the range bins are quite narrow, the radar system is unable to resolve two detected aircraft that are within 10 to 15 deg of each other at the same range bin. The R-RANSAC tracking algorithm is designed to take into account unresolved

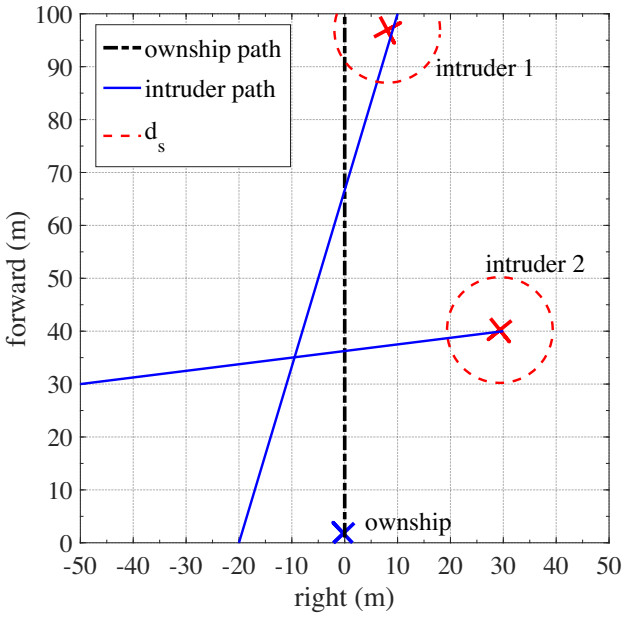

Fig. 9 Encounter geometry of ground-based SAA flight test.

measurements of multiple targets.

As shown in Figure 8(b), the radar processing system consists of four printed circuit boards. These boards are (bottom to top): (1) the RF transmitter and receivers, (2) the IF amplification and filtering, (3) the A/D converters, and (4) the digital signal processing and control board. In the flight test, the radar measurement is sampled 4096 times at a sampling frequency of 2.048 MHz. To increase the SNR, we averaged correlation matrices across 32 time steps. In addition, to remove the background clutter we collected 400 noise measurements using a variable probability of false alarm from 0.03 at the near range bins to 0.15 at the far range bins.

The initial encounter geometry of the flight test is shown in Figure 9. A snap shot at the start of flight test is shown in Figure 10. The initial intended paths of the ownship and the intruders are shown with dashed black and solid blue lines, respectively. In the flight test, we have defined the paths of the ownship and intruders in the NED reference frame, however, the plots of results are shown in the forward-right (FR) reference frame of the radar system. In this configuration, the forward-axis points out the radar antenna, and the right-axis points out the right of the radar system. The orientation of the FR radar reference frame is approximately 73.8 deg relative to north. This specific orientation was due to the physical location of the flight test. For convenience purpose, the collision avoidance path is also shown in the radar FR reference frame. The location of the ground control station and the radar system were obtained with respect to the Global Positioning System (GPS) home location. GPS provided ground truth data for the flight results.

As shown in Figure 9, the ownship starts at $(1, 0)^\top$ in the FR reference frame, with an initial heading of zero degrees measured from the forward direction and follows a straight line path to reach the next waypoint located at $(101, 0)^\top$ m. The ownship flies at a constant speed of 1 m/s. The ground control station is located at $(-2, 0)^\top$ (not shown in the

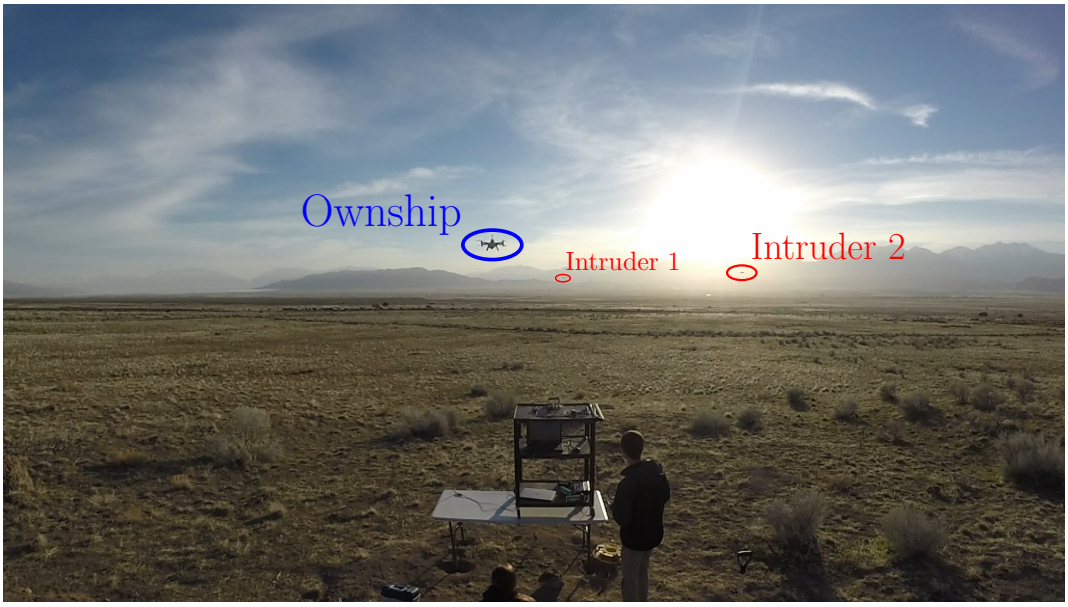

Fig. 10 Ground control station with radar and three aircraft at the start of the test.

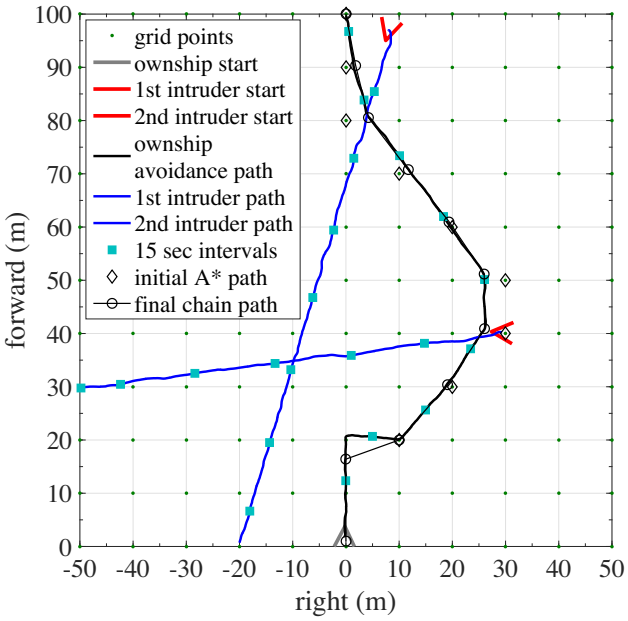

Fig. 11 The avoidance path of the ownship and the paths of the intruders in the FR inertial frame centered about the home location.

figure). Since the avoidance planning is performed in the horizontal plane, the virtual collision volume is reduced to a circle. Because of the small scale of the designed encounter geometry for this flight test, our choice of the collision volume is a scaled-down circular disk of radius $d_s = 10$ m.

The encounter geometry consists of two intruders: one is approaching head-on and the other is converging from the right with respect to the ownship. These intruders follow straight-line paths at a constant speed of 1 m/s. If no collision

avoidance is planned, the d_{cpa} with respect to the first and second intruders is approximately 8 m and 27 m, respectively. Since the d_{cpa} with the first intruder is less than the defined horizontal safety distance d_s, this encounter scenario will lead to a collision. The ownship needs to plan an avoidance maneuver that does not as well lead to a collision with either intruder. Figure 11 shows the intruders' paths and the avoidance path planned by the ownship.

The horizontal distance and time threshold parameters are set to $d_{th} = 100$ m and $\tau_{th} = 10$ s. A detailed description of the collision avoidance algorithm and its design parameters can be found in [19]. The region of the flight test is discretized into grid cells of size 10 by 10 m. Through the implementation of the collision avoidance algorithm, we found it desirable to append certain functionality to increase robustness of the avoidance maneuver. In the A* search algorithm, the cost term is modified to include the time to CPA in the denominator as in [19]

$$c_r = \frac{k_r}{d_{cpa}\tau_{cpa}}. \tag{12}$$

The reason for including τ_{cpa} is primarily to offset the effects of a small d_{cpa} in certain situations. Specifically, if a small d_{cpa} is not expected to occur for an extended period of time, then we should temporarily reduce this cost allowing the ownship greater versatility in its flight path to overcome other threats in the immediate future [19]. An additional cost term is added to Eq. (11) to reward a node that causes the ownship to travel in a direction opposite to the direction of the jth intruder. The objective is to select grid cells which are behind the intruders. The $c_{\mathbf{V}}$ cost term is expressed as [19]

$$c_{\mathbf{V}} = \frac{k_V}{t_{cpa}}(\mathbf{v}_j \odot \mathbf{v}_O), \tag{13}$$

where $\odot$ is the dot product operator, and k_V is a tunable cost parameter. Similarly, an additional force term is added to the chain-based planning algorithm to push the nodes of the chain behind intruder if they come within certain distance the the intruder [19]. The direction that this force is applied is the opposite the direction of the intruder velocity vector, however it does not allow the ownship path to be pushed directly in front of an intruder which would lead to a collision.

Figure 12 shows the range and azimuth angle to all aircraft measured by the radar system. This figure shows that the principal signal decay happens as the azimuth angle increases off boresight as the aircraft leave the antenna beam. The range data, however, remains well resolved for the duration of the test. From this figure we also note that, the measured range has a slight scale factor error compared to the true range to each of the aircraft which could be corrected through further calibration and testing.

As discussed earlier, during the flight test we attempted to orient the radar with a precise heading relative to north, and a specific elevation angle. We also attempted to position the radar at a specific GPS latitude, longitude and altitude location relative to the ground. Although we attempted to position and orient the radar with specific values, errors were unavoidable that resulted in inaccuracies in our measured values when compared to the truth. For ground truth

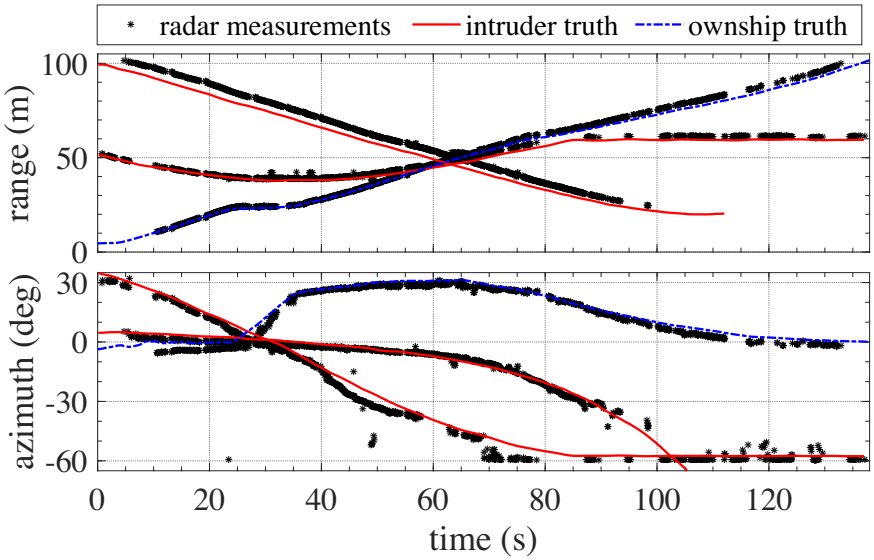

Fig. 12 Radar measurements: range, and azimuth of ownship and intruders.

data, we used the estimated GPS positions of the three aircraft from the Pixhawk autopilot state estimators that also had inaccuracies due to IMU sensor, GPS, and state estimator errors. These errors are further seen in Figure 13, which shows the radar measurements of each aircraft in the FR coordinate frame.

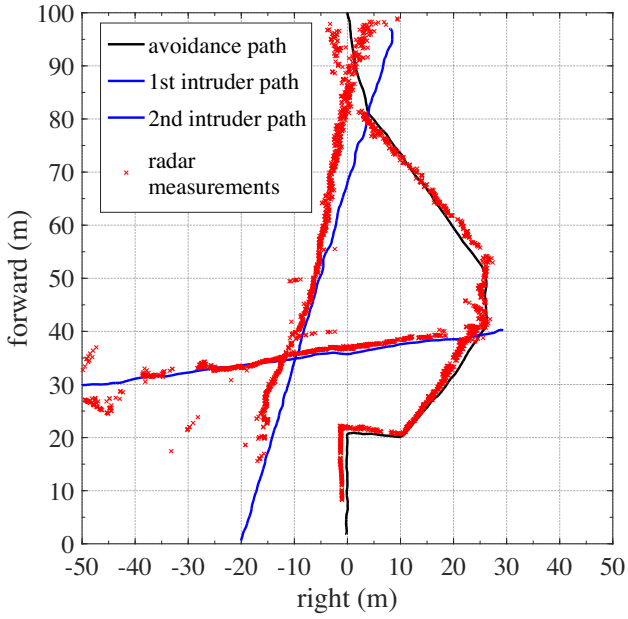

Fig. 13 Aircraft paths constructed using radar measurements.

The state estimates of position and velocity are shown in Figures 14 and 15, respectively. Further details on R-RANSAC implementation and its design parameters for this application are given in [19]. In this flight test, the R-RANSAC algorithm runs at a sample rate of 0.1 s. In the R-RANSAC algorithm, we also chose to implement a

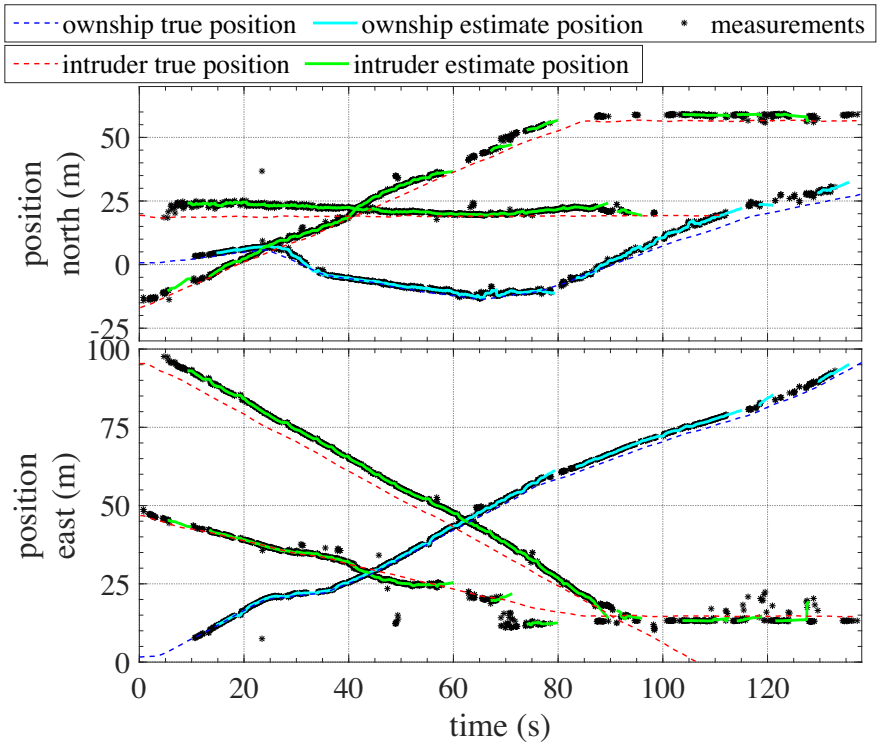

Fig. 14 R-RANSAC tracks: position estimates of aircraft.

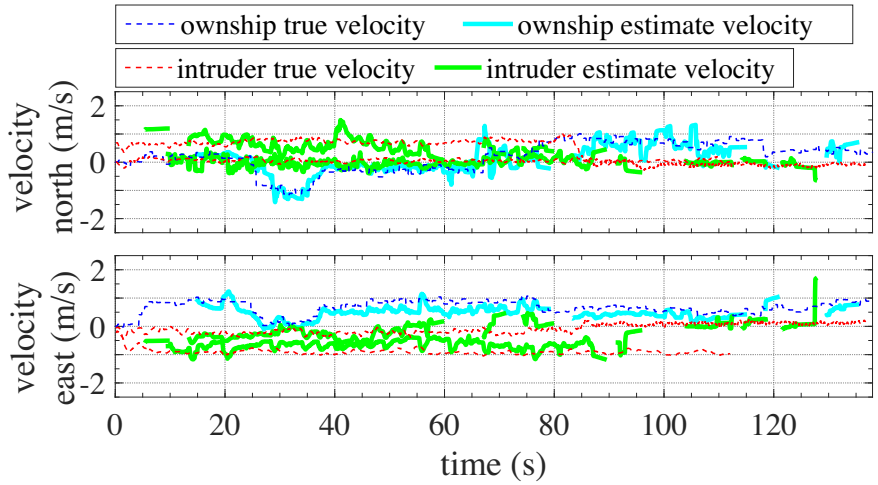

Fig. 15 R-RANSAC tracks: velocity estimates of aircraft.

constant acceleration dynamic model for aircraft. The R-RANSAC algorithm successfully tracks all aircraft as shown in Figures 14 and 15. Additionally, we note that the modifications made to the R-RANSAC algorithm successfully enable it to distinguish the ownship track from the intruder's tracks given that the ownship states are provided from the telemetry link via the 3DR radio. These figures show that the R-RANSAC algorithm takes about 5 s for good models to appear after the initial measurements are received.

The position state estimates of the aircraft are shown in Figure 16. The estimated paths are shown in the radar's FR

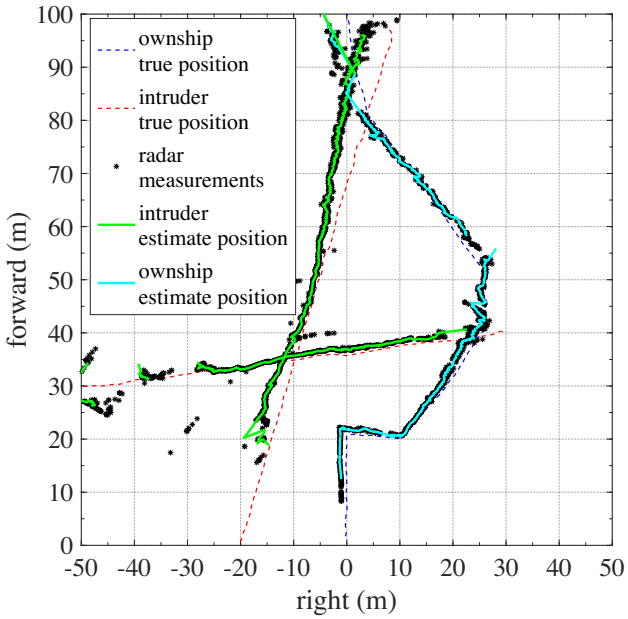

Fig. 16 Aircraft paths constructed using radar measurements and R-RANSAC position estimates.

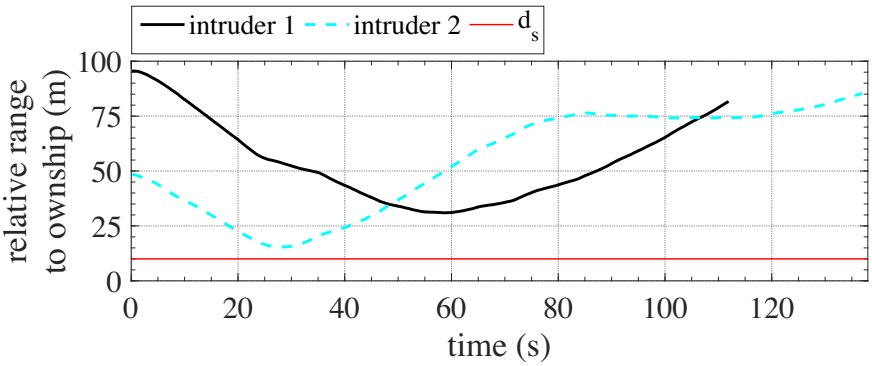

Fig. 17 Relative range to intruders.

reference frame. The R-RANSAC tracks accurately align with the predicted location of the radar measurements.

The relative range between the ownship and the two intruders is shown in Figure 17. For both intruders, the relative range never falls below the safety defined distance d_s which means that no collisions have occurred, and that the ownship successfully planned an avoidance maneuver.

VII. Summary and Conclusions

In this article, we have introduced a ground-based sense-and-avoid system that is feasible for small UAS. We have demonstrated a complete proof-of-concept SAA solution, including a portable and low-cost ground-based radar system, multi-target tracking and estimation, collision detection, and avoidance planning algorithms.

The proposed radar system is a compact phased-array that operates in FMCW mode and exploits state-of-the-art

digital signal processing techniques to drive down the size, weight, power, and cost of the radar design. The digitally steered phased-array radar system described in this paper can track targets simultaneously, while eliminating the need for gimbaled steering or mechanical scanning. In the flight test, the radar system prototype transmitted 250 mW of power, which is sufficient to detect a small-UAS with an RCS of 0.01 m^2 at about 250 m. The radar sensor can detect larger aircraft at approximately 800 m if the target's RCS is 1 m^2 or larger. In general, the radar cross section of the intruder aircraft and the power of the transmitted pulse are two major variables in determining the maximum detection range.

As evident by the flight test results, the R-RANSAC algorithm provides a robust and reliable tracking method that properly exploits radar measurements to track multiple intruders and distinguish them from the ownship in the presence of noisy, cluttered, and missed measurements. The R-RANSAC algorithm provides an increased level of safety and integrity to the SAA system and allows for an adequate time window for the collision avoidance logic to plan an evasive maneuver.

The proposed collision detection algorithm is designed to reduce risk of collisions between aircraft. Using the geometric relationship between aircraft, it estimates the time and distance at the closest point of approach to predict collision alerts that trigger the avoidance algorithm. Linear projections and geometric parameters can be computed efficiently making it a tractable solution for multiple intruders. Moreover, prediction errors are negligible over short look-ahead time windows.

The proposed collision avoidance approach generates solution paths that balance the objectives avoiding collisions and minimizing path length. One of the advantages of our approach is that timing information is specifically embedded in the future path representation of the aircraft, thus allowing the ownship to plan a free-collision path over a wide range of encounter scenarios including multiple intruders and dynamic environments.

ACKNOWLEDGMENTS

This research was conducted in the Center for Unmanned Aircraft Systems (C-UAS) with support from National Science Foundation I/UCRC program grant number IIP-1161036 and C-UAS Industry Advisory Board members.

References

[1] Hottman, S. B., Hansen, K. R., and Berry, M., "Literature Review on Detect, Sense, and Avoid Technology for Unmanned Aircraft Systems," Tech. rep., 2009.

[2] Federal Aviation Administration, "Subchapter F - Air Traffic and General Operating Rules," Tech. rep., 2015.

[3] George, S., "FAA Workshop on Sense and Avoid (SAA) for Unmanned Aircraft Systems (UAS)," , 2009.

[4] Angelov, P., *Sense and Avoid in UAS: Research and Applications*, John Wiley & Sons, Ltd., 2012.

[5] "Standard Specification for Design and Performance of an Airborne Sense-and-Avoid System," Tech. Rep. TR F2411-07, ASTM International, West Conshohocken, PA, 2007.

[6] Lee, S. M., Park, C., Johnson, M. A., and Mueller, E. R., "Investigating Effects of Well Clear Definitions on UAS Sense-And-Avoid Operations," *Aviation Technology, Integration, and Operations Conference*, AIAA, Los Angeles, CA, 2013.

[7] Consiglio, M., Chamberlain, J., Munoz, C., and Hoffler, K., "Concept of Integration For UAS Operations In the NAS," *28th International Congress of the Aeronautical Sciences (ICAS)*, Brisbane, Australia, 2012.

[8] Wilson, M., "Ground-Based Sense and Avoid Support for Unmanned Aircraft Systems," *28th Congress of the International Council of the Aeronautical Sciences*, 2012.

[9] "Guidance Material on Comparison of Surveillance Technologies (GMST)," Tech. rep., International Civil Aviation Organization Asia And Pacific (ICAO), September 2007.

[10] Niedfeldt, P. C., "A Novel Multiple Target Tracking Algorithm in Clutter:Recursive-RANSAC," Ph.D. thesis, Department of Electrical and Computer Engineering, Brigham Young University, June 2014.

[11] Contarino, V. M., and Scire Consultants, L., "All Weather Sense and Avoid System for UASs," Tech. rep., Report to the Office of Naval Research, 2009.

[12] Weber, M. E., "FAA Surveillance Radar Data As A Complement To The WSR-88D Network," *Preprints, 9th Conference on Aviation Range and Aerospace Meteorology*, 2000.

[13] Charvat, G. L., *Small and Short-range Radar Systems*, CRC Press, 2014.

[14] Kemkemian, S., Nouvel-Fiani, M., Cornic, P., and Garrec, P., "MIMO radar for sense and avoid for UAV," *Phased Array Systems and Technology (ARRAY), 2010 IEEE International Symposium on*, IEEE, 2010, pp. 573–580.

[15] Kemkemian, S., Nouvel-Fiani, M., Cornic, P., and Garrec, P., "A Wide Field-of-View Radar for Sense and Avoid on UAV using Space Coloring Waveforms," *Radar Conference (EuRAD), 2010 European*, IEEE, 2010, pp. 220–223.

[16] Itcia, E., Wasselin, J.-P., Mazuel, S., Otten, M., and Huizing, A., "FMCW radar for the sense function of sense and avoid systems onboard UAVs," *SPIE Security+ Defence*, International Society for Optics and Photonics, 2013, pp. 889–914.

[17] Shi, L., Allen, C., Ewing, M., Keshmiri, S., Zakharov, M., Florencio, F., Niakan, N., and Knight, R., "Multichannel Sense-and-Avoid Radar for Small UAVs," *IEEE/AIAA Digital Avionics Systems Conference*, IEEE, 2013.

[18] Richards, M. A., Scheer, J., and Holm, W. A., *Principles of Modern Radar: Basic Principles*, SciTech Publishing, Inc., 2010.

[19] Wikle, J. K., "Integration of a Complete Detect and Avoid System for Small Unmanned Aircraft Systems," Master's thesis, Brigham Young University, 2017.

[20] Niedfeldt, P. C., and Beard, R. W., "Multiple Target Tracking using Recursive RANSAC," *2014 American Control Conference*, 2014, pp. 3393–3398.

[21] Ingersoll, K., Niedfeldt, P. C., and Beard, R. W., "Multiple Target Tracking and Stationary Object Detection using Recursive-RANSAC and Tracker-Sensor Feedback," *Proceedings of the International Conference on Unmanned Air Vehicles*, Denver, CO, 2015.

[22] Quist, E., Niedfeldt, P., and Beard, R. W., "Radar Odometry with Recursive-RANSAC," *IEEE Transactions on Aerospace and Electronic Systems*, Vol. 52, No. 4, 2016, pp. 1618–1630.

[23] Niedfeldt, P. C., and Beard, R. W., "Convergence and Complexity Analysis of Recursive-RANSAC: A New Multiple Target Tracking Algorithm," *IEEE Transactions on Automatic Control*, Vol. 61, No. 2, 2016, pp. 456–461.

[24] Niedfeldt, P. C., Ingersoll, K., and Beard, R. W., "Comparison and Analysis of Recursive-RANSAC for Multiple Target Tracking," *IEEE Transactions on Aerospace and Electronic Systems*, Vol. 53, No. 1, 2017, pp. 461–476.

[25] Blackman, S., and Popoli, R., *Design and Analysis of Modern Tracking Systems*, Artech House, Norwood, MA, 1999.

[26] Bar-Shalom, Y., and Tse, E., "Tracking in a Cluttered Environment with Probabilistic Data Association," *Automatica*, Vol. 11, 1975, pp. 451–460.

[27] Fortmann, T., Bar-Shalom, Y., and Scheffe, M., "Multi-target Tracking using Joint Probabilistic Data Association," *IEEE Conference on Decision and Control*, Vol. 19, 1980, pp. 807–812.

[28] Avitzour, D., "Stochastic Simulation Bayesian Approach to Multitarget Tracking," *IEE Proceedings – Radar, Sonar and Navigation*, Vol. 142, No. 2, 1995, p. 41. doi:10.1049/ip-rsn:19951757.

[29] Mahler, R., "A Theoretical Foundation for the Stein-Winter Probability Hypothesis Density (PHD) Multitarget Tracking Approach," Tech. rep., Lockheed Martin, 2000.

[30] Vo, B.-N., and Ma, W.-K., "The Gaussian Mixture Probability Hypothesis Density Filter," *IEEE Transactions on Signal Processing*, Vol. 54, No. 11, 2006, pp. 4091–4104. doi:10.1109/TSP.2006.881190.

[31] Reid, D., "An Algorithm for Tracking Multiple Targets," *IEEE Transactions on Automatic Control*, Vol. 24, No. 6, 1979, pp. 843–854. doi:10.1109/TAC.1979.1102177.

[32] Adaska, J. W., "Computing Risk For Unmanned Aircraft Self Separation With Maneuvering Intruders," *IEEE Digital Avionics Systems Conference*, 2012.

[33] Weibel, R. E., Edwards, M. W. M., and Fernandes, C. S., "Establishing a Risk-Based Separation Standard for Unmanned Aircraft Self Separation," *Proceedings of the Ninth USA/Europe Air Traffic Management Research & Development Seminar*, Berlin, Germany, 2011.

[34] Temizer, S., Kochenderfer, M. J., Kaelbling, L. P., Lozano-Perez, T., and Kuchar, J. K., "Collision Avoidance for Unmanned Aircraft using Markov Decision Processes," *Proceedings of the AIAA Guidance, Navigation and Control Conference and Exhibit*, 2010.

[35] Geyer, C., Singh, S., and Chamberlain, L., "Avoiding Collisions Between Aircraft: State of the Art and Requirements for UAVs Operating in Civilian Airspace," Tech. Rep. CMU-RI-TR-08-03, Carnegie Mellon University, 2008.

[36] Chen, W., Kay, J., and Raska, V. M., "Autonomous Sense and Avoid (SAA) for Unmanned Air Systems (UAS)," *NATO Research and Technology Organisation (RTO), RTO-SCI-202*, 2009.

[37] Kuchar, J. K., and Yang, L. C., "A Review of Conflict Detection and Resolution Modeling Methods," *IEEE Transactions on Intelligent Transportation Systems*, Vol. 1, No. 4, 2000, pp. 179–189.

[38] Albaker, B. M., and Rahim, N. A., "Unmanned Aircraft Collision Detection and Resolution: Concept and Survey," *IEEE Conference on Industrial Electronics and Applications*, 2010, pp. 248–253.

[39] Geser, A., and Munoz, C., "A Geometric Approach to Strategic Conflict Detection And Resolution," *Proceedings of the 21st IEEE Digital Avionics Systems Conference*, Vol. 1, 2002.

[40] Chiang, Y., Klosowski, J. T., Lee, C., and Mitchell, J. S. B., "Geometric Algorithms for Conflict Detection/Resolution in Air Traffic Management," *Proceedings of the IEEE Conference on Decision and Control*, Vol. 2, 1997, pp. 1835–1840.

[41] Munoz, C., Narkawicz, A., and Chamberlain, J., "A TCAS-II Resolution Advisory Algorithm," *Proceedings of the AIAA Guidance, Navigation, and Control Conference*, Boston, MA, 2013.

[42] Paielli, R. A., and Erzberger, H., "Conflict Probability Estimation for Free Flight," *Journal of Guidance, Control, and Dynamics*, Vol. 20, No. 3, 1997, pp. 588–596.

[43] van Daalen, C. E., and Jones, T., "Fast Conflict Detection using Probability Flow," *Automatica*, Vol. 45, 2009, pp. 1903–1909.

[44] Lauderdale, T. A., "Probabilistic Conflict Detection for Robust Detection and Resolution," *AIAA Aviation Technology, Integration and Operation Conference*, Indianapolis, IN., 2012.

[45] Jackson, J., and Boskovic, J., "Application of Airspace Encounter Model for Prediction of Intruder Dynamics," *AIAA Modeling and Simulation Technologies Conference*, AIAA, 2012.

[46] Lindsten, F., Nordlund, P., and Gustafsson, F., "Conflict Detection Metrics for Aircraft Sense and Avoid Systems," *Proceedings of the IFAC Symposium on Fault Detection, Supervision and Safety of Technical Processes*, Spain, 2009.

[47] Lee, Y., Yang, J. H., Kuchar, J., and Feron, E., "A Real-Time Monte Carlo Implementation for Computing Probability of Conflict," *Proceedings of the AIAA Guidance, Navigation and Control Conference and Exhibit*, Vol. 178, 2004, pp. 1835–1840.

[48] Chryssanthacopoulos, J. P., and Kochenderfer, M. J., "Hazard Alerting Based on Probabilistic Models," *Journal of Guidance, Control, and Dynamics*, Vol. 35, No. 2, 2012, pp. 442–450.

[49] Consiglio, M., Carreno, V., and Williams, D., "Conflict Prevention and Separation Assurance Method in Small Aircraft Transportation System," *AIAA 5th Aviation, Technology, Integration, and Operations Conference (ATIO)*, Arlington, Virginia, 2005.

[50] Cook, S. P., Brooks, D., Cole, R., Hackenberg, D., and Raska, V., "Defining Well Clear for Unmanned Aircraft Systems," *AIAA Infotech@Aerospace*, AIAA, Kissimmee, Florida, 2015.

[51] Sahawneh, L. R., Beard, R. W., Avadhanamz, S., and Bai, H., "Chain-based Collision Avoidance for UAS Sense and Avoid Systems," *AIAA Guidance, Navigation, and Control Conference*, Boston, MA, 2013.

[52] Zeitlin, A. D., "Issues and Tradeoffs in Sense & Avoid for Unmanned Aircraft," *4th Annual IEEE Systems Conference*, 2010, pp. 61–65.

[53] Mejias, L., McNamara, S., Lai, J., and Ford, J., "Vision-Based Detection and Tracking of Aerial Targets for UAV Collision Avoidance," *Proceedings of the IEEE/RSJ International Conference on Intelligent Robots and Systems*, Taipei, Taiwan, 2010, pp. 87–92.

[54] Geyer, M. S., and Johnson, E. N., "3D Obstacle Avoidance in Adversarial Environments for Unmanned Aerial Vehicles," *Proceedings of the AIAA Guidance, Navigation, and Control Confernce and Exhibit*, Keystone, Colorado, 2006.

[55] Yu, H., and Beard, R. W., "A Vision-based Three-tiered Path Planning and Collision Avoidance Scheme for Miniature Air Vehicles," *International Journal of Robotics and Automation*, Vol. 30, No. 5, 2015.

[56] Hoffmann, G. M., Tomlin, C. J., Hoffman, G. M., and Tomlin, C. J., "Decentralized Cooperative Collision Avoidance for Acceleration Constrained Vehicles," *Proceedings of the IEEE Conference on Decision and Control*, Cancun, Mexico, 2008, pp. 4357–4363.

[57] Watanabe, Y., Calise, A. J., Johnson, E. N., and Evers, J. H., "Minimum-Effort Guidance for Vision-Based Collision Avoidance," *Proceedings of the AIAA Atmospheric Flight Mechanics Conference and Exhibit*, American Institute of Aeronautics and Astronautics, Keystone, Colorado, 2006.

[58] Sigurd, K., and How, J. P., "UAV Trajectory Design Using Total Field Collision Avoidance," *Proceedings of the AIAA Guidance, Navigation and Control Conference*, 2003.

[59] Sahawneh, L. R., Argyle, M., and Beard, R. W., "3D Path Planning for Small UAS operating in low-altitude airspace," *Proceedings of the International Conference on Unmanned Aircraft Systems (ICUAS)*, Arlington, VA, 2016.

[60] LaValle, S. M., *Planning Algorithms*, Cambridge University Press, 2006.

[61] Roberts, A. K., "Improvements, Algorithms and a Simulation Model for a Compact Phased-Array Radar for UAS Sense and Avoid," Master's thesis, Brigham Young University, 2017.

[62] Spencer, J. C., "A Compact Phased Array Radar for UAS Sense and Avoid," Master's thesis, Brigham Young University, 2015.

[63] Sahawneh, L. R., Mackie, J., Spencer, J., Beard, R. W., and Warnick, K. F., "Airborne Radar-based Collision Detection and Risk Estimation for Small Unmanned Aircraft Systems," *Journal of Aerospace Information Systems*, Vol. 12, No. 12, 2015, pp. 756–766.